P-ISSN 1991-8941
E-ISSN 2706-6703
Vol. 20, No. 1 (2026)

Journal of University of Anbar for Pure Science
(JUAPS)

journal homepage: juaps.uoanbar.edu.iq

Open Access

Original Paper

Synthesis of copper-doped zinc ferrite thin films via electric field-enhanced spray pyrolysis for visible-light photodetection

Laith Shaker Mahmood[1*], **Mazin A. Alalousi**[2]

[1]College of Science, Department of Physics, University of Anbar, Ramadi, Iraq
[2]Nanomaterials Research Center, University of Anbar, Ramadi, Iraq

ARTICLE INFO

Received: 16/06/2025
Accepted: 24/08/2025
Available online: 21/03/2026
April Issue
10.37652/juaps.2025.161624.1444

Cite @ JUAPS

Corresponding author
Laith Shaker Mahmood
lai22s2010@uoanbar.edu.iq

ABSTRACT

In this work, copper-doped zinc ferrite $Cu_xZn_{1-x}Fe_2O_4$ thin films with x ranging from 0 to 0.09 were synthesized by electric-field-enhanced spray pyrolysis, a novel and successful technique for depositing this cubic-structured material system. The films' structural, morphological, and optoelectronic properties were characterized in detail by X-ray diffraction (XRD), photoluminescence (PL) spectroscopy, field-emission scanning electron microscopy (FE-SEM) imaging, and current–voltage (I-V) measurements to assess their overall suitability as visible-light photodetectors. XRD analyses confirmed a polycrystalline cubic spinel structure. Blue-to-near-infrared emission peaks were observed in PL spectra, and shifts associated with variations in crystallite size and defect states were considered. I-V measurements confirmed improved photoconductivity under illumination, with the best performance at x = 0.05, showing the highest photosensitivity (50.6%) and responsivity (3.39×10^{-4} A/W). Although high doping caused agglomeration and cracking, FE-SEM images showed improved particle uniformity at lower copper concentrations. The films were better suited for detecting blue light, showing their highest sensitivity at 420 nm. By optimizing composition to improve performance, these results highlight the potential of Cu-doped zinc ferrite thin films for optoelectronic devices, particularly photodetection. This work also describes how copper doping enhances the structural and functional characteristics of spinel ferrites for advanced technological applications.

Keywords: *$Cu_xZn1_{-x}Fe_2O_4$, Electric field-enhanced spray pyrolysis, Photoluminescence, Photodetector, Raman shift*

1 INTRODUCTION

Photodetectors are optoelectronic sensors that detect incident light or optical power and convert optical signals into corresponding electrical signals [1]. Photodetectors are used in a broad range of applications, including, but not limited to, optical communication systems, image detection, information processing in optoelectronics, medical diagnostics and imaging, environmental monitoring and detection, and defense and military applications [2]. Among all photodetectors, ferroelectric photodetectors are one of the most researched topics in recent years due to their distinct material properties. In conventional photovoltaic devices, such as p–n junction or metal–semiconductor junction-based devices, photogenerated charge-carrier separation is governed by an intrinsic built-in electric field of the semiconductor material. In contrast, ferroelectric photovoltaic materials utilize the electric field generated by their intrinsic spontaneous polarization to facilitate photoexcited carrier separation and transport. This new mechanism holds promise for future photodetection technologies [3].

Among spinel ferrites, Cu–Zn ferrites exhibit a tunable bandgap [4]. Prior studies indicate that these systems face several challenges when used as photodetectors, including bandgap constraints, charge recombination, Fermi-level

This is an open-access article under CC BY 4.0

© 2026 *The Author(s).* Published by College of Science, University of Anbar.

pinning, and defect density [5–7]. Additionally, operation under a DC current bias has been reported [8].

Spinel-structured ferrites are the most widely used in electrical engineering due to their magnetic properties, which are employed in contemporary electrical engineering [9]. These ferrites exhibit high magnetic permeability and electrical resistance, making them particularly suitable for inductors, sensors, and low- and high-frequency circuits. In addition, their low eddy-current losses make them suitable for magnetic and humidity sensors, filter circuits, and transformers [10–12]. Apart from their desirable electromagnetic characteristics, ferrites are low-cost, stable, small in size, and have a high quality factor, making them ideal base materials for electronic devices in this frequency range [13, 14]. Spinel ferrites adopt the AB_2O_4 structure, where A sites accommodate divalent cations (Ni^{2+}, Zn^{2+}, Cu^{2+}) and B sites contain trivalent cations (Fe^{3+}, Cr^{3+}) [15, 16]. These materials possess a face-centered cubic (FCC) spinel structure, with Cu–Zn ferrites exhibiting very strong magnetic behavior. The magnetic and structural characteristics of these ferrites are a function of the relative proportion of Cu^{2+} and Zn^{2+} because Cu^{2+} substitution affects cation distribution and magnetic ordering within the spinel lattice [17, 18].

Various synthesis pathways, such as sonochemical, solvothermal [19], co-precipitation [20], sol–gel auto-combustion [21], spray pyrolysis [22], and hydrothermal [21], have been reported. The spray pyrolysis method is simple, fast, convenient, efficient, and low-cost. The preparation technique, dopant type, and dopant concentration affect the structural and optical properties of spinel ferrites. Current research on $Cu_xZn_{1-x}Fe_2O_4$ spinel ferrites indicates that copper-type doping is an important factor in altering structural and optical properties. Awad et al. [23] synthesized $Cu_xZn_{1-x}Fe_2O_4$ via a low-temperature combustion method. They observed that while particle size increased, the lattice constant and combustion temperature decreased with increasing Cu^{2+} content. Next, using Moringa oleifera extract (MOE), Komal Yadav et al. [24] prepared copper-doped zinc ferrite nanoparticles via a green method. They confirmed that particle size is influenced by the Cu^{2+} content. The sol-gel self-combustion process was also used by Jamdade et al. [25]to create copper-doped zinc ferrite $Cu_xZn_{1-x}Fe_2O_4$ (x = 0.1, 0.2, 0.3, 0.4, 0.5, 0.6, and 0.7). Nonetheless, there is a direct correlation between copper concentration and porosity and structural parameters. In contrast, Harisha et al. [26] found that particle size increased with increasing copper content despite decreasing lattice parameters. Ankam et al. [5] studied the system $Cu_xZn_{1-x}Fe_2O_4$ and reported that the structural and optical properties are directly affected by copper content at x values of 0, 0.25, 0.5, 0.75, and 1.

The objective of this research is to synthesize copper-substituted zinc ferrite $Cu_xZn_{1-x}Fe_2O_4$, where x = 0 to 0.09, and examine its structural properties at room temperature using electric field-enhanced spray pyrolysis, where the electric field is used to increase the deposition efficiency; this is a novel and successful technique for depositing this cubic-structured material system. To the best of the authors' knowledge, the application of the electric-field-assisted spray pyrolysis technique for preparing ferrite materials of the formula $Cu_xZn_{1-x}Fe_2O_4$ and their use as visible-light photodetectors has not been reported elsewhere in the literature. The technique should lead to the further development of spinel ferrite-based photodetectors, which are increasingly needed for technological and medical applications.

2 MATERIALS AND METHODS

The following precursors were used: cupric nitrate trihydrate ($Cu(NO_3)_2 \cdot 3H_2O$), zinc acetate ($Zn(CH_3COO)_2$), and ferric nitrate nonahydrate ($Fe(NO_3)_3 \cdot 9H_2O$). These chemicals were supplied by Loba Chemie Pvt. Ltd. and Thomas Barker (UK), respectively.

2.1 Preparation of solutions

Aqueous precursor solutions were prepared by dissolving $Cu(NO_3)_2 \cdot 3H_2O$ (2.416 g) (0.1 M), $Zn(CH_3COO)_2$ (2.195 g) (0.1 M), and $Fe(NO_3)_3 \cdot 9H_2O$ (4.040 g) (0.1 M) in 100 mL of deionized water for each solution. The solutions were then mixed in the ratios listed in Table 1.

Table 1 The ferrite compound solution $Cu_xZn_{1-x}Fe_2O_4$, (x=0,-0.09)

value (x)	Composition	$(Cu(NO_3)_2 \cdot 3H_2O)$ (ml)	$((CH_3 \cdot COO)_2 Zn \cdot 2H_2O)$ (ml)	$Fe(NO_3)_3 \cdot 9H_2O$ (ml)
0	$ZnFe_2O_4$	0	25	25
0.01	$Cu_{0.01}Zn_{0.99}Fe_2O_4$	0.25	24.75	25
0.03	$Cu_{0.03}Zn_{0.97}Fe_2O_4$	0.75	24.25	25
0.05	$Cu_{0.05}Zn_{0.95}Fe_2O_4$	1.25	23.75	25
0.07	$Cu_{0.07}Zn_{0.93}Fe_2O_4$	1.75	23.25	25
0.09	$Cu_{0.00}Zn_{0.91}Fe_2O_4$	2.25	22.75	25

2.2 Synthesis of ferrites

Thin films of $Cu_xZn_{1-x}Fe_2O_4$ were prepared by electric field-enhanced spray pyrolysis on n-type silicon substrates with <100> orientation and 1^{-10} Ω·cm (1.5 cm × 1.5 cm). The optimized substrate temperature was 350

© 2026 *The Author(s).*

CC BY 4.0

± 10 °C, the distance between the nozzle opening and the substrate was calibrated to 30 cm, and an electric field of 5 kV was established between the nozzle opening and the substrate. Compressed air was used as a carrier gas. Prior to deposition, the substrates were cleaned using a hydrofluoric acid solution and deionized water in an ultrasonicator. The cleaned substrates were dried in air and used for spray deposition. The deposition process consisted of 15-second spray intervals followed by 15-second pauses. Next, the prepared films were annealed at 500 °C for 30 minutes. Figure 1 illustrates the schematic diagram of the electric field-enhanced spray pyrolysis technology and its associated equipment. The reaction is expected to follow the following chemical equation: Six thin films of copper-doped zinc ferrite were synthesized according to the value of (x).

$$x\mathrm{Cu}\,(\mathrm{NO_3})_2 \cdot 3\mathrm{H_2O} + (1-x)\mathrm{Zn}\,(\mathrm{CH_3COO})_2 \cdot 2\mathrm{H_2O} + 2\mathrm{Fe(NO3)3} \cdot 9\mathrm{H_2O} \rightarrow \mathrm{Cu}_x\mathrm{Zn}_{1-x}\mathrm{Fe_2O_4} + (23-2x)\mathrm{H_2O} + (x+3)\mathrm{N_2} + 2(1-x)\mathrm{CO_2}$$

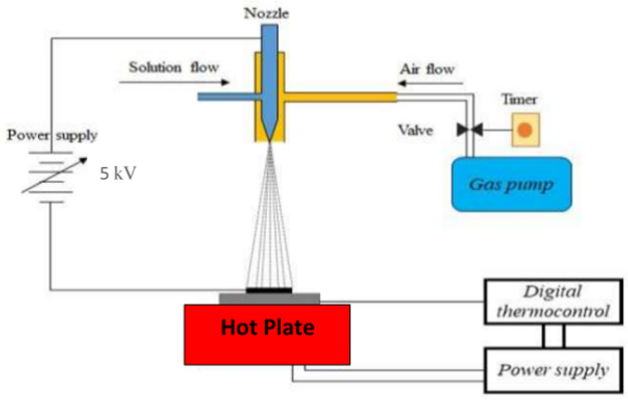

Fig. 1 Schematic diagram of the electrical field–enhanced spray pyrolysis system setup

The structural properties of the ferrite were examined by X-ray diffraction (XRD) at ambient temperature. The diffraction angle was measured from 10 to 90 degrees at a scanning velocity of 0.05 degrees per second. Cu Kα radiation with a wavelength of 1.5405 Å was employed. In addition, photoluminescence spectra were measured from 0 to 900 nm.

For I–V characterization and evaluation of the photodetectors' behavior, aluminum grid electrodes (thickness about 250 nm) were deposited using a vacuum evaporation system. Figure 2 illustrates a diagram of the deposited electrode and a photograph of the system used.

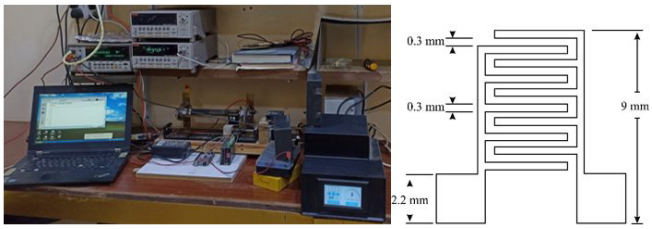

Fig. 2 A diagram of the deposited electrode and a photograph of the used system

In addition, the photosensitivity of the prepared films was tested to determine the optimal wavelength for use as a photodetector in the 200–800 nm range using a single-wavelength variable light source. Optimal performance was found in the blue region, and a 450 nm blue laser source with an intensity of 50 mW/cm^2 was used under an AC bias of 3.5 V. The I–V (dark and light) characteristics were also studied using 30 mW/cm^2 halogen light.

3 RESULTS AND DISCUSSION

The XRD patterns, shown in Figure 3, indicate that $\mathrm{Cu_xZn_{1-x}Fe_2O_4}$ films exhibit a polycrystalline cubic spinel structure. The (111), (220), (311), (400), (422), (333), and (440) planes are represented by peaks at specific angles (2θ) of 18.06°, 29.57°, 34.96°, 42.56°, 52.88°, 56.44°, and 62.63°, respectively. The dominant phase across all prepared samples is 311, which is related to the $\mathrm{ZnFe_2O_4}$ system according to the ICDD 01-082-1049 database. The crystal size was estimated using the Williamson–Hall (W–H) relation and ranged from 14.154 nm to 94.81 nm, as shown in Table 2. To express the cumulative stress-induced and volumetric stress at the hkl diffraction peak, Equation 1 was used; this equation is commonly used to account for strain effects that can change the crystallite size. The volumetric strain and cumulative strain-induced strain at the hkl diffraction peak can be represented by Equation 1 [27].

$$B_{hkl} = (\beta_{hkl})\, D_{hkl} + (\beta_{hkl})\, \varepsilon \qquad (1)$$

where D_{hkl}(nm) is the crystallite size, β_{hkl} is the full width at half maximum (FWHM) of the diffraction peaks and ε is the strain.

The crystallite size was determined using the

© 2026 *The Author(s).* CC BY 4.0

Williamson-Hall (W-H) Equation 2 [28]

$$\cos\theta\beta_{hkl} = \left(\frac{A\lambda}{D_{hkl}}\right) + (4\varepsilon\sin\theta) \quad (2)$$

where (A) denotes the dimensionless shape factor (0.9) and θ (rad) is the diffraction angle.

Increasing the copper ion concentration induces pronounced structural changes, including variations in crystallite size and microstrain, as a consequence of site-occupation preference and ion redistribution. Cu^{2+} ions preferentially occupy octahedral positions, whereas Zn^{2+} occupies tetrahedral positions [29]. With increasing concentration, Cu^{2+} can migrate from octahedral to tetrahedral sites, generating strain due to incomplete replacement [30]. This correlation is supported by the XRD data (Table 2), where the shift in diffraction angle increases proportionally with the strain value [31]. Specifically, for x = 0 (2θ = 34.93°), compressive strain (-0.085%) yields crystallites of 20.92 nm. Incorporation of Cu^{2+} at x = 0.01 (2θ = 35.23°) increases strain (0.159%) and crystallite size (40.83 nm) as Cu^{2+} occupies octahedral sites. The maximum strain (0.135%) at x = 0.05 (2θ = 34.83°) is synchronized with Zn^{2+} migration into tetrahedral sites [29], decreasing the crystallite size (16.25 nm). Stable occupancy at x = 0.07 (2θ = 35.28°) achieves the minimum strain (-0.026%) with improved stability (21.89 nm crystallites). Conversely, Cu dominance at x = 0.09 (2θ = 35.22°) triggers recrystallization (66.13 nm crystallites) with high strain (0.321%). Interestingly, the composite strain is again moderate, suggesting that the material accommodates these site-local redistributions effectively.

FE-SEM images of $Cu_xZn_{1-x}Fe_2O_4$ thin films over a compositional range (x = 0 to 0.09) are shown in Figure 4. Smaller spherical particles (1 µm average diameter) coexist with large, irregular agglomerates in the highly heterogeneous morphology of the $ZnFe_2O_4$ (x = 0) film. Several particles exhibit necking characteristics (neck diameter 200 nm), indicating thermally induced coalescence into larger structures (up to 5.4592 µm). Weak grain connectivity and possible phase segregation are indicated by this morphology. Although the average particle size drops to 600 nm, a similar pattern is observed at x = 0.01. Interestingly, agglomerates as big as 2.8 µm are developed when interparticle coalescence increases, without the clear development of evident necks. The remarkable morphological change occurs at x = 0.03; the film exhibits an excellent, uniform distribution of spherical microparticles and nanoparticles, with much lower agglomeration and improved substrate smoothness. Such enhanced dispersion implies that low-level Cu substitution supports desirable nucleation and growth kinetics. When the Cu content is increased further (x = 0.05), the surface becomes smoother, and quasi-spherical particles are a sign of coalescence. However, with thermal stress development during annealing, higher substitutions (x = 0.07 and 0.09) lead to evident agglomeration and crack formation. Cracks serve as defect sites or recombination foci inside the material. When charge carriers (electrons and holes) produced by light absorption interact with these defect-laden areas, they are more prone to non-radiative recombination instead of contributing to the photocurrent. This diminishes the quantum efficiency of the photodetector, leading to a reduced photocurrent production and decreased responsivity (Figures 4e–f).

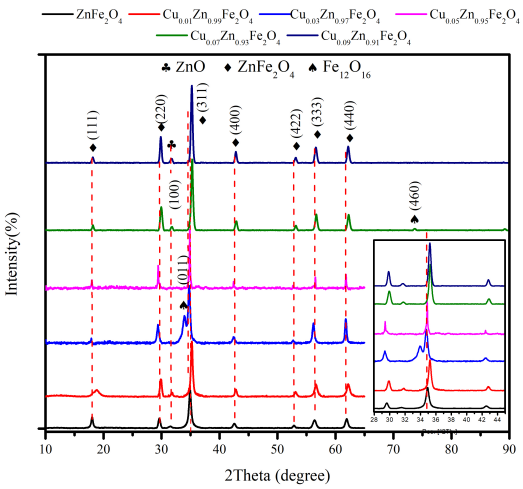

Fig. 3 XRD Diffraction Patterns of $Cu_xZn_{1-x}Fe_2O_4$(x = 0, 0.01, 0.03, 0.05, 0.07, 0.09)

Table 2 XRD data analysis of $Cu_xZn_{1-x}Fe_2O_4$ x=(0,0.01,0.03,0.05,0.07,0.09)

No.	[2Th.]°	d-spacing [Å]	hk1	FWHM [°2Th.]]	Cryst. Size [nm]	Lattice strain [%]	Chemical formula
X = 0	34.93	2.56	311	0.46	20.92	-0.0852	$ZnFe_2O_4$
X = 0.01	35.23	2.54	311	0.32	40.83	0.159	$ZnFe_2O_4$
X = 0.03	34.78	2.57	311	0.41	32.04	0.209	$ZnFe_2O_4$
X = 0.05	34.83	2.57	311	0.61	16.25	0.135	$ZnFe_2O_4$
X = 0.07	35.28	2.54	311	0.4	21.89	-0.026	$ZnFe_2O_4$
X = 0.09	35.22	2.54	311	0.36	66.13	0.321	$ZnFe_2O_4$

© 2026 *The Author(s).*

CC BY 4.0

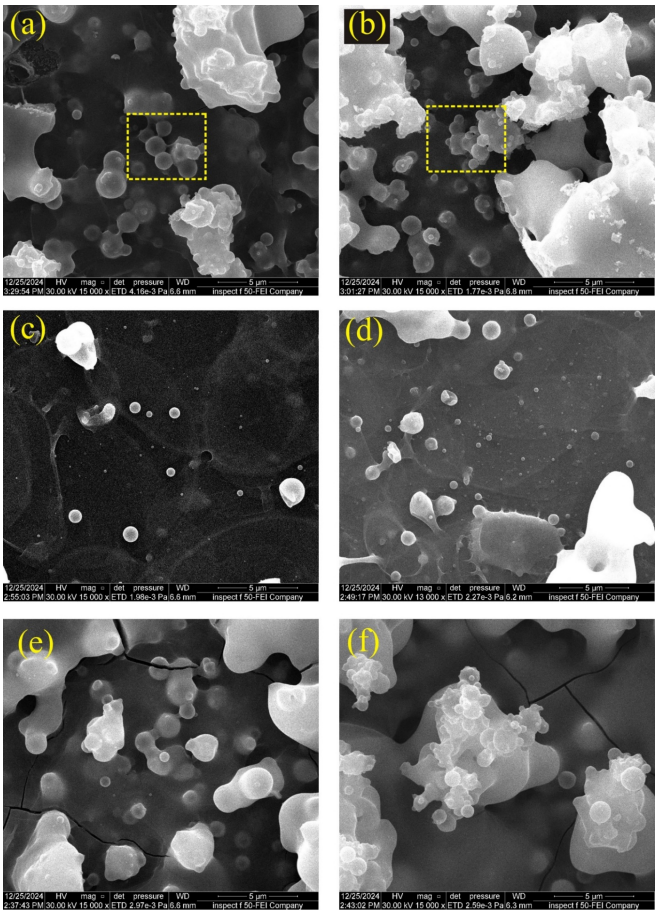

Fig. 4 FE-SEM images of $Cu_xZn_{1-x}Fe_2O_4$, the prepared films

The photoluminescence (PL) properties of $Cu_xZn_{1-x}Fe_2O_4$ films are strongly influenced by their chemical composition, which modifies both the crystal structure and electronic transitions. The PL spectra exhibit five distinct peaks across compositions (x = 0-0.09), as illustrated in Figure 5 and Table 3. In the absence of Cu^{2+}, a dominant emission appears at 445.7 nm in the blue region. With increasing Cu^{2+} concentration, this peak shifts further into the blue, reflecting changes in crystallite size that enhance quantum-confinement effects and correlate with direct bandgap transitions spanning 3.6–2.8 eV [32, 33].

Peaks in the 511-545 nm range are attributed to radiative recombination at octahedral sites, specifically Fe^{3+}: T2g → Eg transitions [33]. The disappearance of these peaks at higher Cu concentrations (x = 0.09) indicates an altered cation distribution within the lattice.

A prominent emission at 365 nm is characteristic of direct band-to-band transitions, where electrons in the valence band recombine with holes in the conduction band, emitting photons with energy close to the bandgap [33]. In oxide materials such as ferrites, this near-ultraviolet peak signifies intrinsic transitions between the main energy bands. For $Cu_xZn_{1-x}Fe_2O_4$, the persistence of this peak suggests robust radiative recombination, underpinned by high crystalline quality and effective band alignment. Doping-induced strain or compositional changes can shift the exact position of this peak, reflecting adjustments in the electronic structure as Cu substitutes for Zn [5]. These features are particularly valuable for optoelectronic applications requiring efficient light emission or absorption in the UV-near-visible range. As noted above, peaks in the 511–545 nm range are attributed to radiative recombination at octahedral sites (Fe^{3+}: $T_{2g} \rightarrow E_g$), and their disappearance at x = 0.09 reflects an altered cation distribution within the lattice.

Substituting Cu for Zn increases the optical bandgap, for example, from 1.8 eV in pure $ZnFe_2O_4$ to approximately 2.8 eV in Cu-doped samples. The augmentation of the optical bandgap with the substitution of Cu for Zn is predominantly ascribed to the Burstein-Moss effect, resulting from an elevated carrier concentration that displaces the absorption edge to higher energies. The 512 nm peak (≈2.42 eV), located in the green region, is commonly associated with exciton recombination or transitions involving defect states such as oxygen vacancies or cation disorder. Mid-wavelength emissions (575–674 nm) are linked to oxygen vacancies and electrons trapped at tetrahedral sites [5, 34]. Variations in intensity, such as the enhanced peak at x = 0.05- correlate with structural distortions induced by Cu^{2+} substitution, which also affects Fe^{3+} occupancy in octahedral sites. Longer-wavelength peaks (737–860 nm) are attributed to deep-level defects, including Fe^{2+}/Fe^{3+} inter-valence charge transfer and infrared transitions. The gradual disappearance of the 860 nm peak with increasing Cu content indicates suppressed oxygen-vacancy formation, as Cu^{2+} stabilizes the spinel lattice [5].

Pure $ZnFe_2O_4$ (x = 0) adopts a cubic spinel structure, while higher Cu concentrations (x ≥ 0.5) result in tetragonal distortion [5, 35]. This phase transition alters cation distribution, with Zn^{2+} preferentially occupying tetrahedral sites and Fe^{3+} octahedral sites, thereby modifying PL emission pathways [36]. The optical bandgap increases with Cu substitution (e.g., from 1.825 eV for x = 0 to 2.776 eV for x = 1), consistent with the blue shift observed in the 445.7 nm peak. Higher Cu content also reduces the density of oxygen vacancies, diminishing the intensities of certain peaks.

© 2026 *The Author(s).*

CC BY 4.0

Increasing Cu content in $Cu_xZn_{1-x}Fe_2O_4$ films shifts PL peak positions due to changes in the crystal field and defect states, and can either enhance or reduce PL intensity depending on whether Cu introduces additional radiative centers or non-radiative pathways [36–38]. The specific behavior of the 512 nm peak, which shifts or disappears with increasing Cu, highlights its strong dependence on the local environment and defect structure.

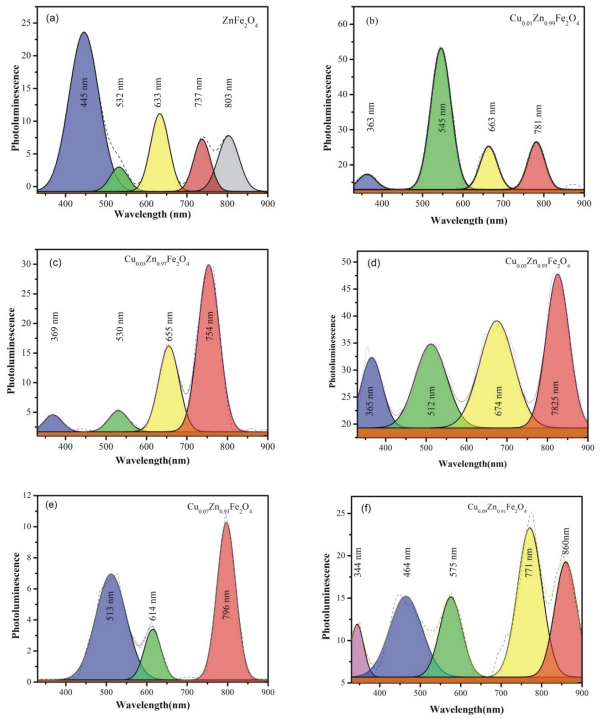

Fig. 5 The photoluminescence peaks of the $Cu_{n2}Zn_{(1-x)}Fe_2O_4$ films

Table 3 The photoluminescence peaks of the $Cu_xZn_{1-x}Fe_2O_4$ films

X=0 (nm)	Intensity (a.u.)	X= 0.01 (nm)	Intensity (a.u.)	X= 0.03 (nm)	Intensity (a.u.)	X= 0.05 (nm)	Intensity (a.u.)	X= 0.07 (nm)	Intensity (a.u.)	X= 0.09 (nm)	Intensity (a.u.)
445	24.3	363	17.3	369	4.5	365	32.3			344	11.9
532	3.7	545	53.3	530	5.3	512	34.7	512	6.9	464	15.16
633	11.8	663	25.3	655	16.2	674	39	614	3.4	575	15.1
737	7.9	781	26.5	754	29.9			796	10.27	771	23.3
803	8.5					825	47.8			860	19.27

Figure 6 presents I–V (current–voltage) plots illustrating the electrical performance of $Cu_xZn_{1-x}Fe_2O_4$ thin films under dark and illumination (light) conditions for various copper concentrations (x = 0, 0.01, 0.03, 0.05, 0.07, 0.09). For all compositions, the current under illumination (red line) is higher than in the dark (black line) at any voltage. This indicates clear photoconductive behavior, demonstrating that the films are photosensitive and generate additional charge carriers under illumination. The curves are roughly symmetrical about the origin, suggesting near-ohmic contacts and uniform film properties across the voltage range. $Cu_xZn_{1-x}Fe_2O_4$ films display enhanced current under illumination for all copper concentrations, with a sharp peak in photoconductive response at x = 0.05. This implies that precise adjustment of copper concentration can effectively influence the material's prospects for utilization in optoelectronic devices such as photodetectors.

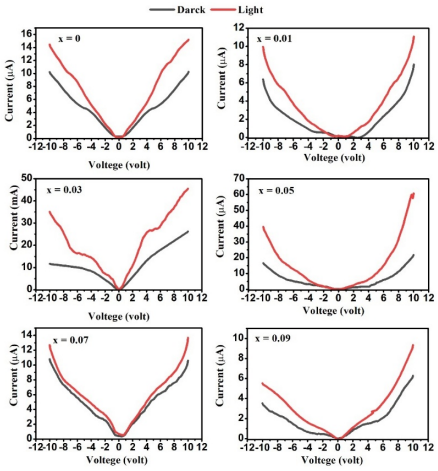

Fig. 6 Dark and light I-V characterization of $Cu_xZn_{1-x}Fe_2O_4$, x = 0 – 0.09

Figure 7 illustrates the wavelength-dependent Photoresponse of the films ranging from 200 to 700 nm. The optimized wavelength was around 420 nm.

The experimental findings, as shown in Figure 8 and Table 4, demonstrate a clear trend in the photodetection performance of $Cu_xZn_{1-x}Fe_2O_4$ thin films as a function of copper content (x = 0–0.09). More specifically, Figure 8a shows that the photodetection performance of the films at a wavelength of 450 nm improves systematically with increasing copper-ion concentration. Figure 8b also shows that the photosensitivity (S%) of the films increases with copper content up to a certain extent. It attains optimal performance at x = 0.05, likely due to the electronic structure's design and the introduction of localized states, which enable more efficient absorption and charge transport under illumination [39,40]. It then begins to deteriorate with increasing Cu^{2+} content due to the formation of cracks, which increase at x = 0.07 and 0.09.

© 2026 *The Author(s).*

CC BY 4.0

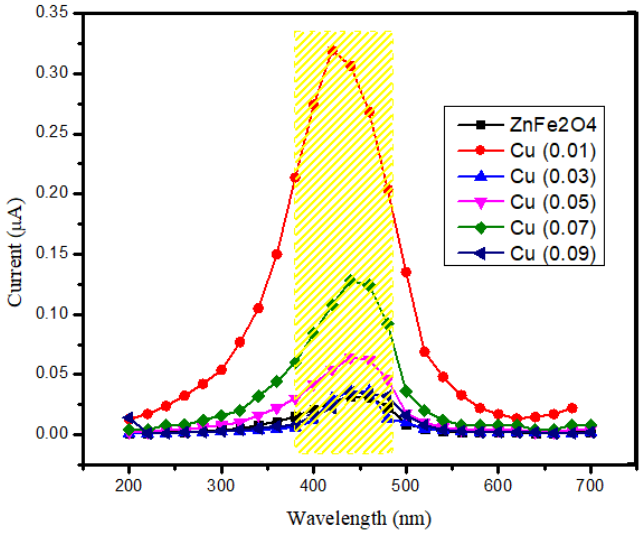

Fig. 7 The sensing of the prepared films to various wavelengths

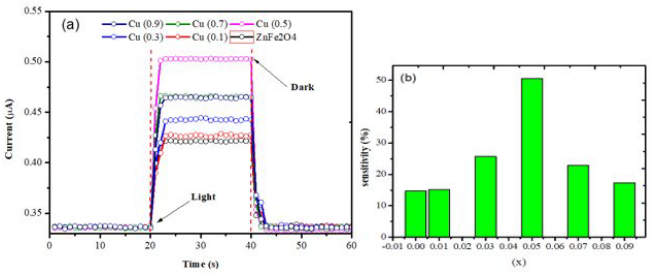

Fig. 8 (a) Photodetector behavior for various x, (b) the Photodetector sensitivity

These enhancements are consistent with previous work on ferrite and oxide transition-metal-doped films, where cation substitution (e.g., Co or Cu) has been observed to improve photodetector performance by increasing carrier mobility and reducing recombination rates. For example, $ZnFe_2O_4$-doped thin films exhibited high photosensitivity and fast response times to visible light, confirming that targeted doping is an effective strategy for optimizing photodetector materials [41,42].

These results confirm the potential of $Cu_xZn_{1-x}Fe_2O_4$ films as efficient visible-light photodetectors. The monotonic increase in photosensitivity and sensitivity with increasing copper concentration indicates that careful composition engineering can be used to tune the optoelectronic properties of such ferrite films for device applications. However, over-doping can eventually lead to defect states that act as recombination centers and hamper further improvements, a trend observed in similar oxide systems [39–42].

Table 4 The Photodetector parameters

x	photo current (μA)	$J \times 10^{-6}$ (A/cm^2)	$R_\lambda \times 10^{-4}$ A/W	η (%)	NEP $\times 10^{-9}$ (W)	D $\times 10^8$	D* $\times 10^8$ (Jones)	Sensitivity (%)
0	0.866	2.89	5.78	0.20 5	1.32	7.55	1.55	14.7
0.0 1	0.704	2.35	4.69	0.16 6	1.49	6.69	1.40	15.2
0.0 3	0.425	1.42	2.84	0.10 0	2.07	4.83	1.14	25.7
0.0 5	0.508	1.69	3.39	0.12 0	1.89	5.29	1.35	50.6
0.0 7	0.711	2.37	4.74	0.16 8	1.79	5.59	1.43	22.8
0.0 9	0.895	2.98	5.97	0.21	1.52	6.58	1.59	17.3

4 CONCLUSION

Electric field-assisted spray pyrolysis is a powerful, easy, and affordable method for depositing copper-doped zinc ferrite ($Cu_xZn_{1-x}Fe_2O_4$, x = 0–0.09) films. I–V measurements confirmed improved photoconductivity under illumination in copper-doped samples. The $Cu_{0.05}Zn_{0.95}Fe_2O_4$ film achieved a responsivity of 3.39×10^{-4} A/W, surpassing undoped $ZnFe_2O_4$ by 2×, demonstrating the effectiveness of controlled Cu doping. Cu^{2+} substitution introduces compressive strain and promotes crystallite growth, which can significantly affect the optical and possibly magnetic properties of the synthesized Cu–Zn ferrite, even though it has no discernible effect on the crystal-structure phases.

$Cu_xZn_{1-x}Fe_2O_4$ thin films are suitable for optoelectronic applications under limiting conditions where strict control over lattice strain and crystallinity is essential because their structural and microstructural properties are influenced by the ratio of Cu^{2+} ions. Further studies could explore doping with other transition metals (e.g., Ni, Co) to enhance responsivity beyond 10^{-3} A/W and suggest these films as promising materials for photodetection and advanced technological applications.

Acknowledgement

N/A

Funding source

No funds received.

Data availability

N/A

DECLARATIONS

Conflict of interest

No conflict of interest.

© 2026 *The Author(s).*

CC BY 4.0

Consent to publish

N/A

Ethical approval

N/A

REFERENCES

[1] Wang XX, Zeng G, Yu QJ, Shen L, Shi CY, Lu HL. Photodetectors integrating waveguides and semiconductor materials. Nanoscale. 2024;16(11):5504–5520. 10.1039/d4nr00305e

[2] Wu Y, Fukuda K, Yokota T, Someya T. A Highly Responsive Organic Image Sensor Based on a Two-Terminal Organic Photodetector with Photomultiplication. Advanced Materials. 2019;31(43). 10.1002/adma.201903687

[3] Lee YM, Lu YY, Fu CT, Kuo CT, Hou LC, Chuang YH, et al. Manganese Copper Ferrite Thin Films for Visible–Near-Infrared Region Photodetector Applications. physica status solidi (RRL) – Rapid Research Letters. 2022;16(7). 10.1002/pssr.202200074

[4] Balaraman S, Iruson B, Krishnmoorthy S, Elayaperumal M. In: The Presented Study of Zn-Cu Ferrites for Their Application in "Photocatalytic Activities". IntechOpen; 2021. 10.5772/intechopen.99535

[5] Ankam V RL Karka G. Structural and Optical Properties of Copper-Doped Zinc Ferrites Using Solid State Reaction Method. Materials International. 2025;7(1):1. 10.33263/materials71.001

[6] Liu Y, Hsu J, Fu Y, Tsai K. Preparation of Cu–Zn ferrite photocatalyst and it's application. International Journal of Hydrogen Energy. 2016;41(35):15696–15702. 10.1016/j.ijhydene.2016.04.127

[7] Guijarro N, Bornoz P, Prévot M, Yu X, Zhu X, Johnson M, et al. Evaluating spinel ferrites MFe2O4 (M = Cu, Mg, Zn) as photoanodes for solar water oxidation: prospects and limitations. Sustainable Energy & Fuels. 2018;2(1):103–117. 10.1039/c7se00448f

[8] Zhu J, Zhu Y, Chen Z, Wu S, Fang X, Yao Y. Progress in the Preparation and Modification of Zinc Ferrites Used for the Photocatalytic Degradation of Organic Pollutants. International Journal of Environmental Research and Public Health. 2022;19(17):10710. 10.3390/ijerph191710710

[9] Aman S, Ahmad N, Alhossainy MH, Albalawi H, Morsi M, Al-Muhimeed TI, et al. Structural, magnetic, electrical and microwave properties of spinel ferrites. Journal of Rare Earths. 2022;40(3):443–450. 10.1016/j.jre.2021.04.015

[10] Azam A. Microwave assisted synthesis and characterization of Co doped Cu ferrite nanoparticles. Journal of Alloys and Compounds. 2012;540:145–153. 10.1016/j.jallcom.2012.06.068

[11] Devi N, Pal Y, Ahmed N, Sharma V, Sharma N. Synthesis & Characterization of Magnetic Properties of Cu-Zn Nano Ferrites. Journal of Emerging Technologies and Innovative Research. 2022;9(5):b428-32. Available from: https://www.jetir.org/papers/JETIR2205159.pdf

[12] Luo F, Duan Z, Zhang Y, Shang Y. Influence of microstructure optimization on magnetic and thermal properties of MnZn ferrite. Journal of Materials Science: Materials in Electronics. 2021;32(12):15633–15642. 10.1007/s10854-021-06112-0

[13] Kumar N, Singh D, Nigam A, Rajpoot O, Kumar M, Yadav, et al. Structural and magnetic properties of zinc doped copper ferrite synthesized by sol-gel and hydrothermal route. Materials Physics and Mechanics. 2021. 10.18149/MPM.4722021_12

[14] Srivastava R, Yadav BC. Ferrite Materials: Introduction, Synthesis Techniques, and Applications as Sensors. International Journal of Green Nanotechnology. 2012;4(2):141–154. 10.1080/19430892.2012.676918

[15] Sözeri H, Deligöz H, Kavas H, Baykal A. Magnetic, dielectric and microwave properties of M–Ti substituted barium hexaferrites (M=Mn2+, Co2+, Cu2+, Ni2+, Zn2+). Ceramics International. 2014;40(6):8645–8657. 10.1016/j.ceramint.2014.01.082

[16] Qamar S, Akhtar MN, Batoo KM, Raslan EH. Structural and magnetic features of Ce doped Co-Cu-Zn spinel nanoferrites prepared using sol gel self-ignition method. Ceramics International. 2020;46(10):14481–14487. 10.1016/j.ceramint.2020.02.246

[17] Rathod SM, Chavan AR, Jadhav SS, Batoo KM, Hadi M, Raslan EH. Ag+ ion substituted CuFe2O4 nanoparticles: Analysis of structural and magnetic behavior. Chemical Physics Letters. 2021;765:138308. 10.1016/j.cplett.2020.138308

© 2026 *The Author(s).*

CC BY 4.0

[18] Tatarchuk T, Bououdina M, Macyk W, Shyichuk O, Paliychuk N, Yaremiy I, et al. Structural, Optical, and Magnetic Properties of Zn-Doped CoFe2O4 Nanoparticles. Nanoscale Research Letters. 2017;12(1). 10.1186/s11671-017-1899-x

[19] Saleem A, Zhang Y, Gong H, Majeed MK, Lin X, Hussain MM, et al. Electromagnetic wave absorption performance of Ni doped Cu-ferrite nanocrystals. Materials Research Express. 2020;7(1):016117. 10.1088/2053-1591/ab6c1a

[20] Manzoor T, Javed T, Mustafa G, Manzoor Ahmed HU, Razzaq A. Facile synthesis of CuxZn1-xFe2O4 nanoparticles and their thermo-physical properties evaluation. Applied Physics A. 2019;125(9). 10.1007/s00339-019-2917-x

[21] Dhyani R, Srivastava RC, Rawat PS, Dixit G. Structural and elastic properties of tetragonal nano-structured copper ferrite. International Journal of Materials Research. 2022;113(10):884–892. 10.1515/ijmr-2021-8552

[22] Chaudhari MN. Thin film Deposition Methods: A Critical Review. International Journal for Research in Applied Science and Engineering Technology. 2021;9(VI):5215–5232. 10.22214/ijraset.2021.36154

[23] Awad HM, El-Maghraby A. PREPARATION, STRUCTURE AND CATALYTIC ACTIVITY OF SIMPLE SPINEL AS NANO-COPPER-ZINC FERRITES IN INDUSTRY MODEL. Rasayan Journal of Chemistry. 2018;11(3):1320–1327. 10.31788/rjc.2018.1133086

[24] Yadav K, Ahmed G, Chauhan H. Green synthesis of Cu-doped zinc nano fer-rite materials using Moringa oleiferaleaves. Journal of Indian Research. 2022;10(3&4):57

[25] JAMDADE S, TAMBADE P, RATHOD S. Study of variation in porosity and its associated parameters due to Cu doping in zinc ferrite using sol-gel autocombustion method. UPB Scientific Bulletin, Series. 2024

[26] HARISHA G, THEJAS R, PADMINI BV, DEVARAJA CR, MURUGENDRAPPA MV, RAJASHEKARA KM. Structural, morphological, magnetic, and dielectric properties of copper-substituted Cu_XZn_$(1-X)$Fe_2O_4 nanoparticles: Green synthesis. Journal of Metals, Materials and Minerals. 2024;34(3):1955. 10.55713/jmmm.v34i3.1955

[27] Jahil SS, Mohammed IA, Khazaal AR, Jasim KA, Harbbi KH. Application the Halder – Wagner to Calculation Crystal Size and Micro Strain by X-ray Diffraction Peaks Analysis. NeuroQuantology. 2022;20(1):199–204. 10.14704/nq.2022.20.1.nq22074

[28] Mittemeijer EJ, Welzel U. In: The "state of the art" of the diffraction analysis of crystallite size and lattice strain. OLDENBOURG WISSENSCHAFTSVERLAG; 2008. p. 99–100. 10.1524/9783486992564-013

[29] Maria KH, Choudhury S, Hakim MA. Structural phase transformation and hysteresis behavior of Cu-Zn ferrites. International Nano Letters. 2013;3(1). 10.1186/2228-5326-3-42

[30] Al gasani L, Alalousi M. Properties Investigation of Fullerene/GNPs Composite Films. Journal of University of Anbar for Pure Science. 2024;18(2):180–187. 10.37652/juaps.2024.146514.1188

[31] Yau JK. Evaluation of crystallite size and strain from X-ray diffraction pattern. 1988

[32] Akhter S, Paul DP, Hakim MA, Saha DK, Al-Mamun M, Parveen A. Synthesis, Structural and Physical Properties of Cu1-xZnxFe2O4 Ferrites. Materials Sciences and Applications. 2011;02(11):1675–1681. 10.4236/msa.2011.211223

[33] Rathore MS, Verma H, Akhani SB, Pathak J, Joshi U, Joshi A, et al. Photoluminescence and antibacterial performance of sol–gel synthesized ZnO nanoparticles. Materials Advances. 2024;5(8):3472–3481. 10.1039/d3ma01096a

[34] Ahmadova SA, Naghiyev TG, Aliyeva SN, Sadigova AA, Mehdiyev TR, Javid H. Photoluminescence properties of Ni1xZnxFe2O4 nanopowders; 2019.

[35] Kumar GSY, Naik HSB, Roy AS, Harish KN, Viswanath R. Synthesis, Optical and Electrical Properties of ZnFe2O4 Nanocomposites. Nanomaterials and Nanotechnology. 2012;2:19. 10.5772/56169

[36] Bedia FZ, Bedia A, Bedia SM, Maloufi N, Aillerie M, Rahmoun K. Enhancing visible luminescence in sprayed-ZnO nanostructure through Cu doping. AIP Advances. 2025;15(1). 10.1063/5.0237396

[37] Peng WQ, Cong GW, Qu SC, Wang ZG. Synthesis and photoluminescence of ZnS:Cu nanoparticles. Optical Materials. 2006;29(2–3):313–317. 10.1016/j.optmat.2005.10.003

© 2026 *The Author(s).*

CC BY 4.0

[38] Shiratori D, Masai H, Kato T, Okada G, Nakauchi D, Kawaguchi N, et al. Oxidation suppression of Cu in alkaline aluminophosphate glass and the effects for radiation-induced luminescence characteristics. Scientific Reports. 2020;10(1). 10.1038/s41598-020-78510-z

[39] T-R C. American Chemical Society (ACS);. 10.1021/acsami.0c20487.s001

[40] Singh M, Ambedkar AK, Tyagi S, Kumar A, Kumar A, Gautam YK, et al. Enhanced Visible-Light Photodetection with Undoped and Doped ZnO Thin-Film Self-Powered Photodetectors. ACS Omega. 2023;8(40):36966–36977. 10.1021/acsomega.3c04091

[41] Nawaz MN, Ghazanfar U, Yuan W, Wahab H, Satti OT, Khan SB. Impact of cobalt doping on the properties of zinc ferrite (CoxZn1-xFe2O4). Journal of Materials Science: Materials in Electronics. 2025;36(13). 10.1007/s10854-025-14770-7

[42] Faramawy AM, El-Sayed HM. Enhancement of magnetization and optical properties of CuFe2O4/ZnFe2O4 core/shell nanostructure. Scientific Reports. 2024;14(1). 10.1038/s41598-024-57134-7

How to cite this article

Mahmood LS, Alalousi MA. Synthesis of copper-doped zinc ferrite thin films via electric field-enhanced spray pyrolysis for visible-light photodetection. Journal of University of Anbar for Pure Science. 2026; 20(1):233-242. doi:10.37652/juaps.2025.161624.1444

© 2026 *The Author(s).*

CC BY 4.0